# Chapter 6
# Nonlinear Dynamics of Ambient Noise-Driven Graphene Nanostructured Devices for Energy Harvesting

**A. El Aroudi, M. López-Suárez, E. Alarcón, R. Rurali and G. Abadal**

## 6.1 Introduction

Recently, there has been an increasing of interest in self-powered devices in remote environment applications where energy becomes an important system requirement and the use of rechargeable batteries becomes problematic such as in hard-to-access locations or, because the lifetime of the batteries is much shorter than of that of the system to be powered. Many solutions have been suggested in the literature to remedy this problem by using energy harvesting techniques [1]. Energy harvesting is considered a key factor in the development of autonomous sensors and micro- and nanogenerators with extended lifetimes. There are different energy harvesting technologies that can be used depending on the kind of the available energy. Among the energy sources, vibrational kinetic energy is the most used for applications such as development of microgenerators [1] and noise harvesters for nanosensors [2]. In this approach, mechanical energy is converted to electricity by using piezoelectric, capacitive, or inductive transducers. Vibration-based energy harvesting research has

A. El Aroudi (✉)
University Rovira i Virgili, Tarragona, Spain
e-mail: abdelali.elaroudi@urv.cat

M. López-Suárez · G. Abadal
Universitat Autónoma de Barcelona, Barcelona, Spain
e-mail: miquel.lopez@nipslab.org

G. Abadal
e-mail: gabriel.abadal@uab.cat

E. Alarcón
Universitat Politècnica de Catalunya, Barcelona, Spain
e-mail: eduard.alarcon@upc.edu

R. Rurali
Institut de Ciència de Materials de Barcelona (ICMAB-CSIC),
Campus de Bellaterra, Barcelona, Spain
e-mail: rrurali@icmab.es



E. Blokhina et al. (eds.), *Nonlinearity in Energy Harvesting Systems*,
DOI 10.1007/978-3-319-20355-3_6

largely focused on linear electromechanical devices excited at resonance. To overcome problems related to linear energy harvester working as resonators, nonlinear energy harvesters have been proposed in certain applications [3]. In the nonlinear energy harvesting approach, rather than resonance frequency tuning [4, 5], the nonlinearity of the system is exploited to improve the performances of the energy harvester within a wide frequency range outperforming classical resonant energy harvesters [3, 6]. Energy harvesting can be performed both at the macro-[3], micro-[7] and even at nanoscales [2]. Unfortunately, most of the available power sources have very low frequency oscillations while the resonant frequency of any nano-mechanical device is paradoxically high ($\propto$ GHz) which makes many issues related to their performances as energy harvesters yet to be solved, particularly that of extracting energy at low frequencies. Nonlinearities in energy harvesting nanodevices may play a vital role to solve these issues. Recent works have used nanodevices such as piezoelectric zinc oxide (ZnO) nanowires [8] where mechanical energy coming from light wind and body movement was converted to electrical energy by a coupled piezoelectric-semiconductor process. Due to their extremely low power consumption, nanosystems that harvest their energy from their environment is attractive for applications such as wireless sensing, personal electronics for battery charging, implantable biological devices, biomedical science, and environmental monitoring such as animal migration tracking and gas and chemical species sensing [9–11]. The nanogenerators could also be used to harvest energy created by tire pressure change and mechanical vibration due to moving vehicles [9].

## 6.2 Graphene-Based Nanomaterials for Energy Harvesting

Graphene is a newly discovered nanomaterial that has interesting peculiar electronic and mechanical properties making it a promising candidate for future electronic applications [12]. It consists of a flat monolayer of carbon atoms tightly packed into a two-dimensional honeycomb-like lattice. It can be considered as a building block for graphite materials of all other dimensionality [13]. This material exhibits high conductivity, large surface area, and electrochemical window. All these properties make it an advantageous material for energy storage devices. A literature review concerning the electrochemical application of graphene in energy storage/generation devices can be found in [14]. Some applications of graphene in solar cells, batteries, and fuel cells can be found in [15]. In [16] biosensors and biosensing systems employing graphene have been described.

A review providing a scientific progress of different type of graphene materials is [17]. Their structural, thermal, optical, and electrical properties along with their potential applications and the impact of graphene and related materials on the environment, its toxicological effects and its future prospects have been also discussed.

In [18] it has been shown that a strained nanostructured graphene posses an intrinsic mechanical nonlinearity and it can be used for nonlinear energy harvesting at the nanoscale. There, it has been also shown that when weakly compressed, the graphene

sheet behaves like a double-well system and that for a critical value of the compression ratio, the harvested power is optimal. In [19] some discussions on some recent studies on graphene-based NGs have been provided. In [20], tests involving water flow with various molarities of hydrochloric acid over few-layered graphene are performed and the authors report higher induced voltages for graphene as compared to nanotubes. In [21] graphene oxide films have been fabricated as a low-cost and flexible nanogenerator to convert acoustic energy into electricity with a about of 12 % conversion efficiency.

## 6.3 Chapter Outline

The aim of this chapter is to study the nonlinear dynamic behavior of a strained nanostructured graphene membrane first considered in [18] for possible use in energy harvesting applications. Based on the initial study by the authors that was presented in [22] and [23], in this chapter we thoroughly study and expand the previous analysis and we fully explain the reported phenomena. To accomplish this aim, the rest of the paper is organized as follows. In Sect. 6.2, a brief description of the mathematical model of the graphene harvester is provided. Section 6.3 presents the dynamical behavior of the device in the absence of any external excitation. Equilibrium points and their stability are studied in the same section. In Sect. 6.4, deterministic excitation is considered and the dynamics of the system is studied when the external force intensity and frequency are varied. In Sect. 6.5, the dynamics of the system is studied under a random excitation in the form of a white noise with a Gaussian distribution and a limited bandwidth. In Sect. 6.6, the performances of the system under random excitation are studied in terms of RMS levels. The study is extended in Sect. 6.7 to an array of three graphene membrane-based harvesters. Finally, conclusions are provided in the last section.

## 6.4 Mathematical Model of the Graphene Vibrating Membrane for Energy Harvesting Applications

### *6.4.1 Nonlinear Mathematical Model*

Figure 6.1 shows the system under study in this chapter. It consists of a flat suspended graphene membrane with a compression ratio defined as $\varepsilon = (L_0 - L)/L_0$, where $L$ is the length of the graphene membrane and $L_0$ its equilibrium value in the absence of any compression. Let us consider different values of the compression ratio $\varepsilon$ between 0 % (uncompressed graphene) and 10 %.

Let us suppose that the graphene membrane is submerged in a noisy environment. Let $\xi(t) = \sigma^2\eta(t)$, where $\eta(t)$ is a white noise excitation with a Gaussian distribution

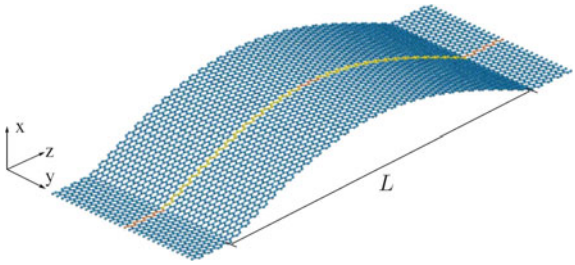


**Fig. 6.1** Uncompressed or weakly compressed graphene membrane [18]

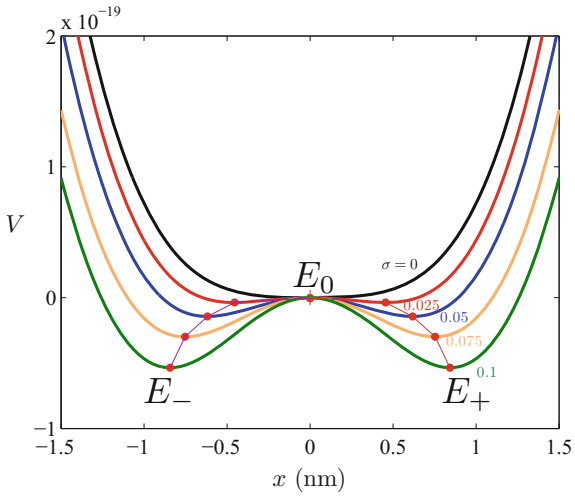


**Fig. 6.2** Potential $V(x)$ for different values of the compression factor $\varepsilon$. For $\varepsilon \neq 0$, equilibrium points are also plotted. $E_+$ and $E_-$ are attractors while $E_0$ is a saddle point

noise whose mean value is zero, its variance is $\sigma^2$. By developing the Euler–Bernoulli equation for clamped beams, the following mass-spring dynamic model is obtained for the considered graphene membrane [18]

$$m\ddot{x} = -\frac{\partial V}{\partial x} - b\dot{x} + \sigma^2\eta(t) \tag{6.1}$$

where $x$ is the displacement, $m$ represents the effective mass of the layer, $b$ stands for the damping factor, and $V(x)$ is the potential energy which is given by [18]

$$V(x) = \frac{1}{56}v_8x^8 + \frac{1}{30}v_6x^6 + \frac{1}{12}v_4x^4 + \frac{1}{2}v_2x^2 \tag{6.2}$$

The potential energy is depicted in Fig. 6.2 for different values of the compression factor $\varepsilon$. Equilibrium points represented by extremum points of $V(x)$ are also plotted in the same figure. For $\varepsilon = 0$, the potential energy corresponds to a harmonic linear oscillator presenting a single equilibrium point $E_0$ at the origin. For $\varepsilon \neq 0$, the points $E_+$ and $E_-$ are minima and therefore they are attractors while $E_0$ is a maximum and corresponds to a saddle point.

**Table 6.1** Coefficients $v_i$ $(i = 2, 4, 6, 8)$ for the potential energy for different values of the compression ratio $\varepsilon$

| $\varepsilon$ | $v_8/56$ | $v_6/30$ | $v_4/12$ | $v_2/2$ |
|---|---|---|---|---|
| 0 | $6.57 \times 10^{50}$ | $-5.73 \times 10^{33}$ | $6.74 \times 10^{16}$ | 0.0096 |
| 0.025 | $1.30 \times 10^{51}$ | $-1.36 \times 10^{34}$ | $9.26 \times 10^{16}$ | −0.036 |
| 0.05 | $2.56 \times 10^{51}$ | $-2.29 \times 10^{34}$ | $1.14 \times 10^{17}$ | −0.078 |
| 0.075 | $2.76 \times 10^{51}$ | $-2.34 \times 10^{34}$ | $1.16 \times 10^{17}$ | −0.112 |
| 0.1 | $3.89 \times 10^{51}$ | $-3.43 \times 10^{34}$ | $1.49 \times 10^{17}$ | −0.165 |

The coefficients $v_i$ $(i = 2, 4, 6, 8)$ are given in Table 6.1 for different values of compression coefficient $\varepsilon$. These values have been obtained by means of ab initio density-functional calculations with the SIESTA code [18, 24], where the graphene sheet is modeled at a fully atomistic level and its electronic structure solved quantum mechanically. Equation (6.1) can be rearranged as follows

$$\ddot{x} = -\frac{b}{m}\dot{x} - \frac{1}{m}\frac{\partial V}{\partial x} + \frac{\sigma^2}{m}\eta(t) \tag{6.3}$$

If we let $v = \dot{x}$. Hence, the previous model can also be written as a set of two first-order differential equation in the state space form

$$\dot{x} = v \tag{6.4}$$

$$\dot{v} = -\frac{b}{m}v - \frac{1}{m}\frac{\partial V}{\partial x} + \frac{\sigma^2}{m}\eta(t) \tag{6.5}$$

whose divergence is

$$\nabla = \frac{\partial \dot{x}}{\partial x} + \frac{\partial \dot{v}}{\partial v} + \frac{\partial \dot{t}}{\partial t} = -\frac{b}{m} \tag{6.6}$$

which is unconditionally negative and therefore the system is dissipative for every set of parameter values.

### 6.4.2 Dynamics of the Unforced System

Before embarking on the study of the noise-driven system, let us consider first, the situation where $\xi(t) = 0$ in such a way that the system is free from any excitation. Under this circumstance the dynamics of the system will depend upon the parameters of the nanodevice. Namely, mass, damping factor, and compression ratio. Let us consider a compressed graphene membrane with compression coefficient $\varepsilon \neq 0$ in such a way that the origin is a saddle point (non-stable).

$$\dot{x} = v \tag{6.7}$$

$$\dot{v} = -\frac{b}{m}v - \frac{1}{m}\frac{\partial V}{\partial x} \tag{6.8}$$

Therefore the model (6.7) and (6.8) has three equilibrium points which are

$$E_0 = (0, 0), \quad E_- = (X_-, 0), \quad E_+ = (X_+, 0) \tag{6.9}$$

where $X_-$ and $X_+$ are the non-null displacement equilibria that can be obtained in closed form. Moreover, one can observe that the potential is symmetric and that if $X_q$ is an equilibrium position $-X_q$ will also be. Therefore one has $X_- = -X_+$. Only real equilibrium points are of practical interest. These equilibrium points can also be obtained by forcing the derivative of $V(x)$ to be zero and solving for $x$. Let us define $\mu$ as follows

$$\mu = 14700v_4v_6v_8 - 94500v_2v_8^2 - 2744v_6^3 + 140v_8\sqrt{5}\sqrt{(3500v_4^3v_8 - 735v_4^2v_6^2 - 28350v_4v_6v_8v_2 + 91125v_2^2v_8^2 + 5292v_2v_6^3} \tag{6.10}$$

Therefore the expressions of the non-null equilibrium points are given by the following expression

$$X_- = -\frac{1}{30v_8\sqrt[3]{\mu}}\sqrt{-30v_8\sqrt[3]{\mu}(14v_6\sqrt[3]{\mu} - \sqrt[3]{\mu} + 700v_4v_8 - 196v_6^2)} \tag{6.11}$$

$$X_+ = \frac{1}{30v_8\sqrt[3]{\mu}}\sqrt{-30v_8\sqrt[3]{\mu}(14v_6\sqrt[3]{\mu} - \sqrt[3]{\mu} + 700v_4v_8 - 196v_6^2)} \tag{6.12}$$

The Jacobian matrix of (6.7) and (6.8) is

$$\mathbf{J} = \begin{pmatrix} 0 & 1 \\ -\frac{1}{m}\frac{\partial^2 V}{\partial x^2} & -\frac{b}{m} \end{pmatrix} \tag{6.13}$$

and the corresponding characteristic polynomial can be expressed as follows

$$p(\lambda, x) = \lambda^2 + \frac{b}{m}\lambda + \frac{1}{m}\frac{\partial^2 V}{\partial x^2} \tag{6.14}$$

The two equilibrium points $E_-$ and $E_+$ with a displacement different from zero will be both attracting since their corresponding Jacobian matrices do not have eigenvalues on the right-half side of the complex plane. For the equilibrium point $E_0$ with null displacement $x = 0$, the characteristic polynomial will have one eigenvalue in the right-half plane and another one in the left side which corresponds to a saddle point. This is a typical situation for double-well systems where two attracting points can

be reached depending on the initial conditions while the separatrix of the saddle point will establish the boundary of the basins of attraction. In the bistable case, the two equilibrium points $E_-$ and $E_+$ are separated by a barrier whose maximum is at $x = 0$ and whose height is $\Delta V = -V(X_+) = -V(X_-)$. The dynamics of the system is mainly characterized by the oscillation around the two minima $X_+$ and $X_-$, and crossing over the potential barrier $\Delta V$. This fact will be exploited by making the displacement to swing between the two minima and accordingly to make the RMS value to increase proportionally to the distance between the equilibrium point which under sufficient excitation intensity, this in turn will imply a maximization of the harvested energy when the system is noise driven [25].

## 6.5 Dynamical Behavior of the Noise-Driven System from Numerical Simulations

Consider now that the system is subject to a random excitation with a normal distribution and a maximum bandwidth $\omega_{\text{bw}}$. When such noise is applied to the system, the probability to swing between the two equilibrium points $X_-$ and $X_+$ increases. Consequently noise can be used to increase the RMS value of the displacement and accordingly to raise the harvested energy. Let us also consider a compressed graphene sheet with compression coefficient $\varepsilon \neq 0$ in such a way that the origin is a saddle point (non stable). The nonlinear model of the system is numerically solved. A MATLAB Simulink model was built for the system equation modeling the graphene nano-harvester device according to the mathematical model given in (6.1). The MATLAB Simulink block diagram used for simulations is shown in Fig. 6.3.

For some specific values of noise level, the system was simulated during 500 ns and the time series, phase space, probability density, and amplitude spectra are plotted. The parameter values used are as follows, damping coefficient $b = 9.9869 \times 10^{-15}$

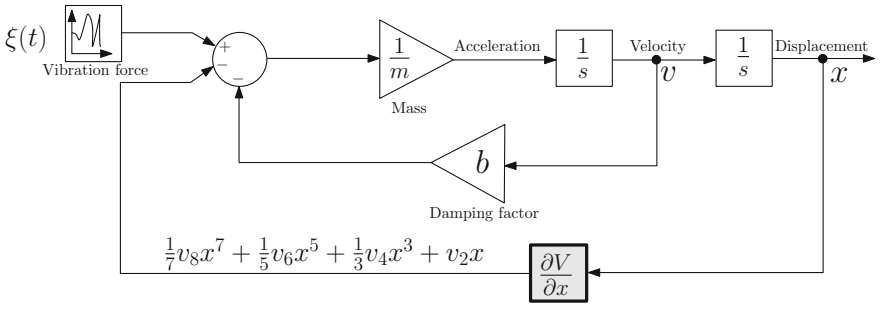


**Fig. 6.3** Simulink block diagram of the graphene membrane

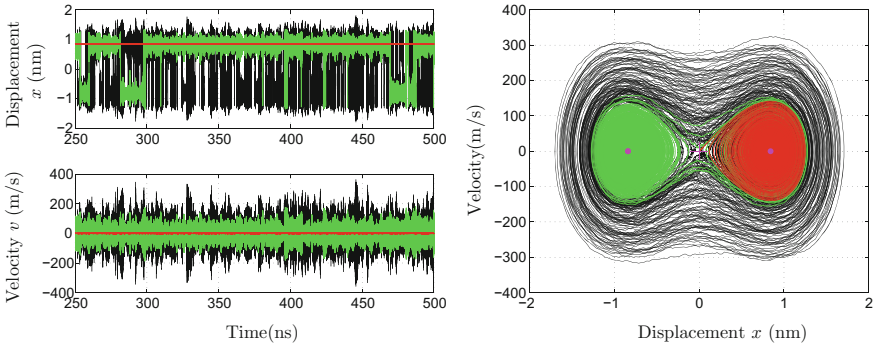


(a) Time series. (b) Phase plane $(x, v)$.

**Fig. 6.4** Dynamics of the graphene membrane under a random excitation $\sigma^2 = 1$ pN (*red*), $\sigma^2 = 50.5$ pN (*green*) and $\sigma^2 = 100$ pN (*black*)

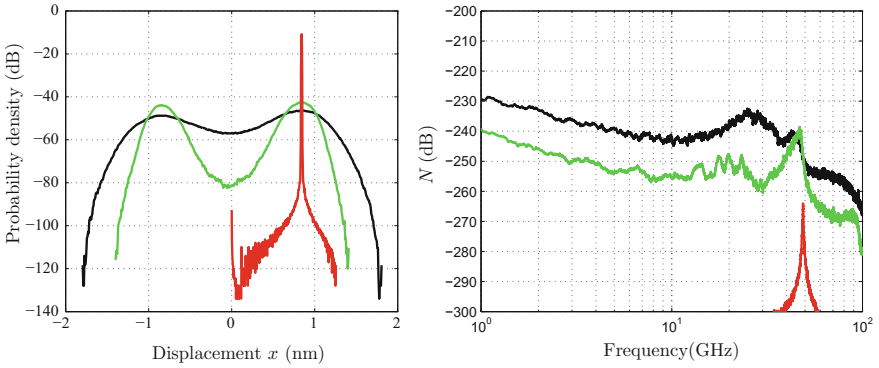


(a) Probability density function of $x$. (b) The FFT of $x$ and $\sigma^2\eta(t)$.

**Fig. 6.5** Spectrum and probability density function corresponding to Fig. 6.4. Note that the spectrum is spread down to low frequency regions when the noise intensity is sufficiently large so that the potential barrier can be crossed

and $m = 5.2982 \times 10^{-24}$. Figures 6.4 and 6.5 show the dynamics of the system for different values of noise strengths. The following particular cases are plotted in these figures

- $\sigma^2 = 1$ pN, the noise intensity is weak and the system evolves to the vicinity of one of the stable equilibrium points $X_-$ or $X_+$ depending on the initial conditions. The probability to swing between the two equilibria is almost zero. The vicinities of $X_-$ and $X_+$ correspond to the unique set with nonzero values of the probability density function. The energy of the system is concentrated in a limited range of frequency near the resonant frequency (≈50 GHz).
- $\sigma^2 = 50.5$ pN, the noise intensity is sufficient to make the barrier to be beat and make the system to leave the vicinity of the stable equilibrium points $X_-$ or $X_+$ swinging between them. The range within which the displacement can be

obtained includes the interval $(X_-, X_+)$. The equilibria $X_-$ and $X_+$ correspond to the maximum of the probability density function.

- $\sigma^2 = 100$ pN, the noise intensity is in such a way that the probability of swinging between the stable equilibrium points $X_-$ or $X_+$ is larger and the system presents larger velocities and displacements and therefore the harvested energy will also be larger.

## 6.6 Performance of the System in Terms of Design Parameters

The RMS value of the displacement and noise amplitude spectra for varying noise level and compression ratio are computed and the amount of power that can be harvested versus noise level and compression ratio are plotted. This power is divided by the corresponding noise amplitude. The results are shown in Fig. 6.6. One can observe in Fig. 6.6a that as the noise level and the compression ratio are increased, the RMS value of the displacement also increases.

Regarding the power that can be harvested, shown in Fig. 6.6b, it can be observed that there is an optimal zone where this ratio is maximal. In particular, it can be noticed that for the linear case ($\varepsilon \approx 0$), the power that can be harvested is low even for relatively high values of the noise level. Nonlinear effects in the device ($\varepsilon \neq 0$), improve the potentials of the device for energy harvesting even at low noise intensity levels. From Fig. 6.6, one can observe that with $\varepsilon \neq 0$, the RMS value of $x$ and therefore the power that can be harvested is always larger than the corresponding linear case ($\varepsilon = 0$)

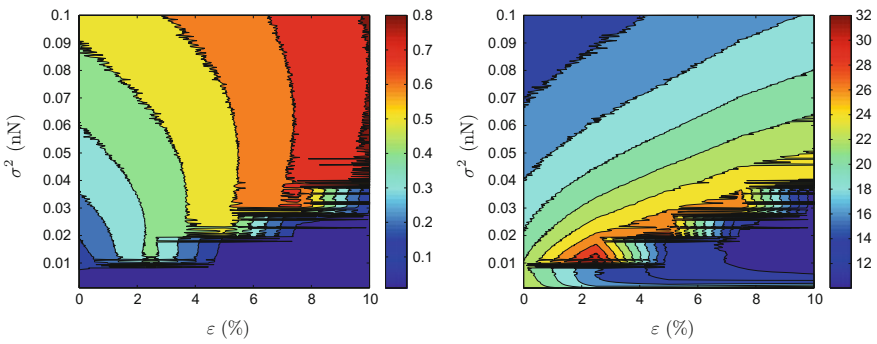


(a) The RMS value of $x$ (in nm) (b) Power/$\sigma^2$ (in dB)

**Fig. 6.6** Performances of the system in terms of $\sigma^2$ and $\varepsilon$

## 6.7 Coupled Graphene Vibrating Membrane for Energy Harvesting

### *6.7.1 Nonlinear Mathematical Model*

We consider four coupled flat suspended graphene sheets with a compression ratio $\varepsilon_i$, effective mass $m_i$ with an equivalent damping factor $b_i$ and a potential energy $V_i, i = 1 \ldots 4$. The equivalent mechanical scheme is shown in Fig. 6.7. The coupled system can be described by the following set of coupled differential equations

$$m_1\ddot{x}_1 = -\left.\frac{\partial V(x)}{\partial x}\right|_{x=x_1} - \left.\frac{\partial V_1(x)}{\partial x}\right|_{x=x_2-x_1} - b\dot{x}_1 + \sigma^2\eta(t) \tag{6.15}$$

$$m_2\ddot{x}_2 = -\left.\frac{\partial V(x)}{\partial x}\right|_{x=x_2-x_3} - b\dot{x}_2 + \left.\frac{\partial V_2(x)}{\partial x}\right|_{x=x_1-x_2} - b\dot{x}_2 \tag{6.16}$$

$$m_3\ddot{x}_3 = -\left.\frac{\partial V(x)}{\partial x}\right|_{x=x_3-x_4} - b\dot{x}_3 + \left.\frac{\partial V_3(x)}{\partial x}\right|_{x=x_2-x_3} - b\dot{x}_2 \tag{6.17}$$

$$m_4\ddot{x}_4 = -\left.\frac{\partial V(x)}{\partial x}\right|_{x=x_4} - b\dot{x}_4 + \left.\frac{\partial V_4(x)}{\partial x}\right|_{x=x_3-x_4} - b\dot{x}_2 \tag{6.18}$$

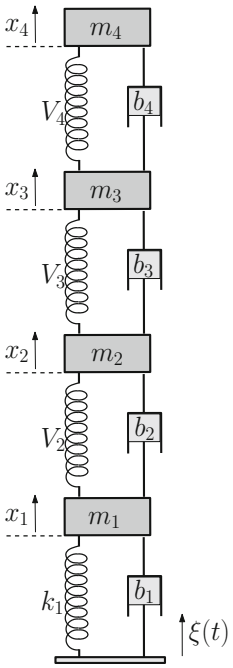


**Fig. 6.7** Mechanical equivalent scheme of three coupled graphene membranes

where $x_i$, $i = 1 \ldots 4$ are the displacements for the coupled graphene membranes, $m_i$ for $i = 1 \ldots 4$ represents the effective mass of each of the layer $i$, $k_i$ its equivalent stiffness and $b_i$ stands for their damping factors. For simplicity it is assumed that all the membranes are identic, i.e., they have the same mass, stiffness, the same damping coefficient and compression ratio and therefore the same potential energy $V$ which is the same one given (6.2).

## 6.8 Dynamics of the Coupled Membranes from Numerical Simulations

In this section, only two values of noise intensity are considered, namely $\sigma^2 = 1$ and 50 pN, and different diagrams in the form of times series, state planes, FFT spectra, and probability density function of the displacement are obtained as for the single membrane case.

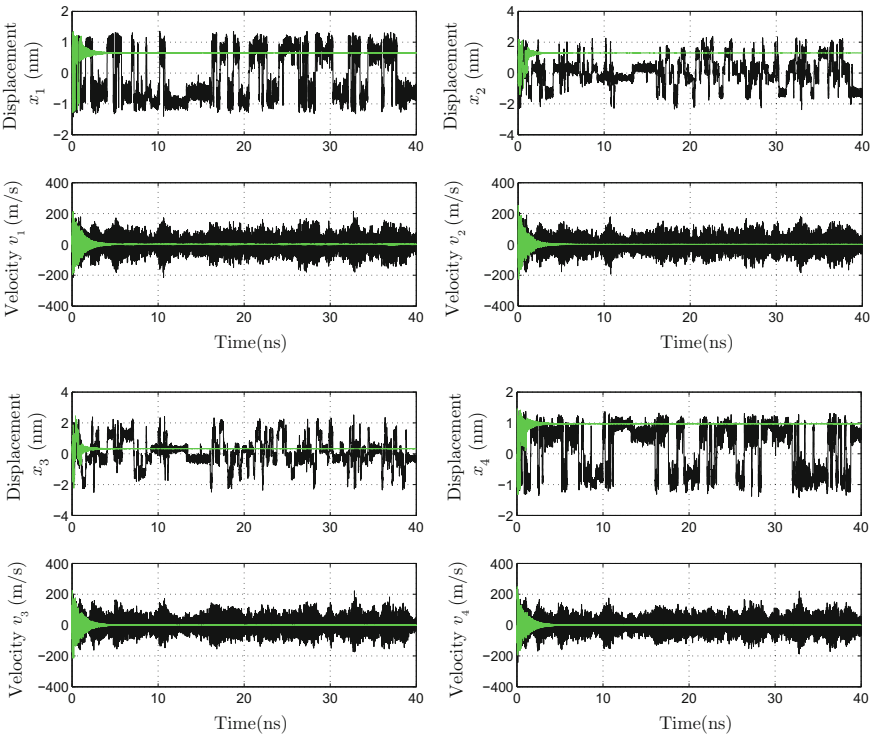


**Fig. 6.8** Time domain waveforms of the displacements $x_i$ and velocities $v_i$, $(i = 1 \ldots 4)$ corresponding to the four graphene membranes for two values of noise intensities

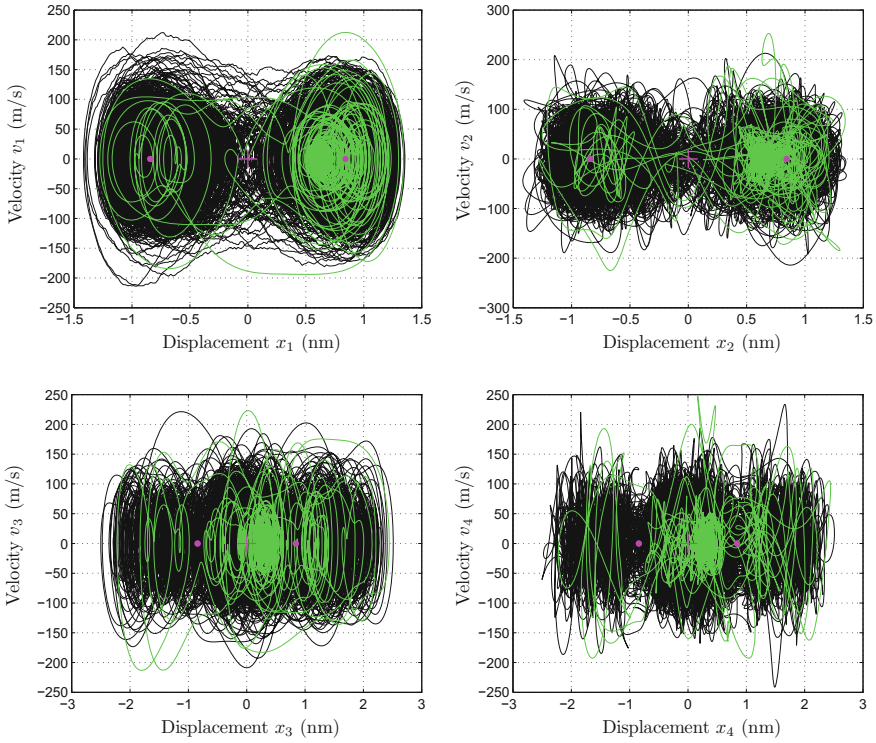


**Fig. 6.9** The state space in the planes $(x_i, v_i)$, $(i = 1 \ldots 4)$ corresponding to the four graphene membranes for two values of noise intensities

Figure 6.8 shows the time domain waveforms of the system. For low values of noise intensity the system stays in the vicinity of the equilibrium point. For low values of noise intensity the system stays in the vicinity of the equilibrium point.

Figure 6.9 shows the projection of the state plane time of the system in the planes $(x_i, v_i)$, $(i = 1 \ldots 4)$ corresponding to each graphene membrane. For relatively high values of noise intensity, the trajectory can only evolve to an equilibrium point being the ambient vibration in this case not sufficient to make the system to oscillate between the two regions. When the noise intensity increases, as in the case of the single membrane, the system trajectory visits more the different equilibrium points and larger oscillation amplitude can be reached. All the four membranes are characterized by the same dynamics.

Figure 6.10 depicts the FFT spectra of the displacement corresponding to each graphene membrane. Since we have a system with four degrees of freedom, four different vibration modes of with different frequencies should appear. While this is the case for the low intensity noise case, the spectrum corresponding to a relatively high value of noise intensity is spread a broad range of frequencies. This occurs for all the membranes.

Figure 6.11 shows the probability density functions calculated for the different displacements of the membranes. For low values of noise intensity, the probability of finding the system in the vicinity of one of its equilibrium points is practically one. For relatively high values of noise intensity, the probability to visit a wider region increases being the maximum probability that corresponding to the vicinity of the equilibrium points.

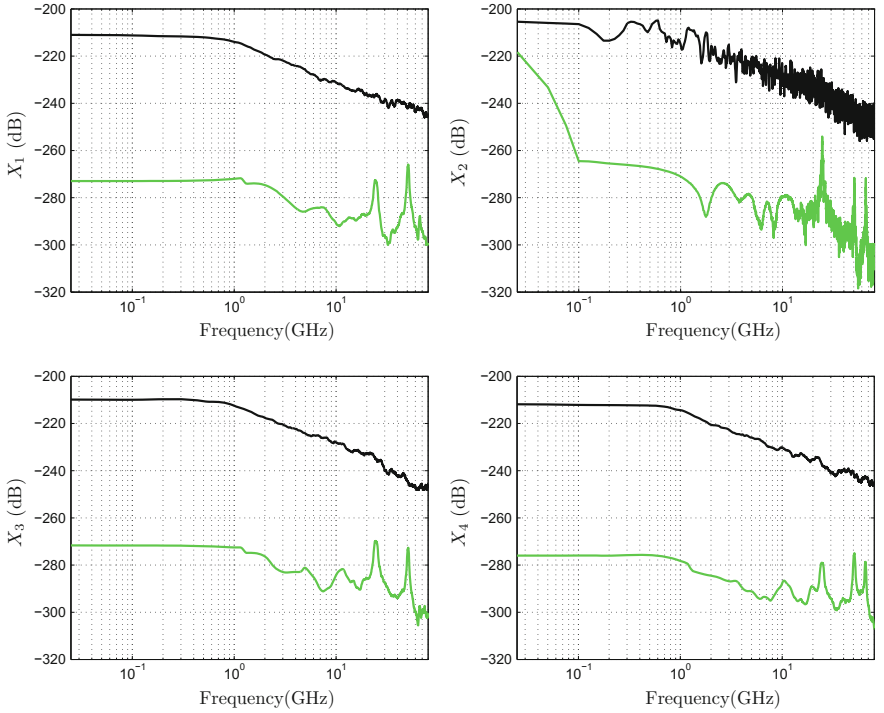


**Fig. 6.10** FFT spectra of the displacements $x_i$ $(i = 1 \ldots 4)$ corresponding to the four graphene membranes for two values of noise intensities

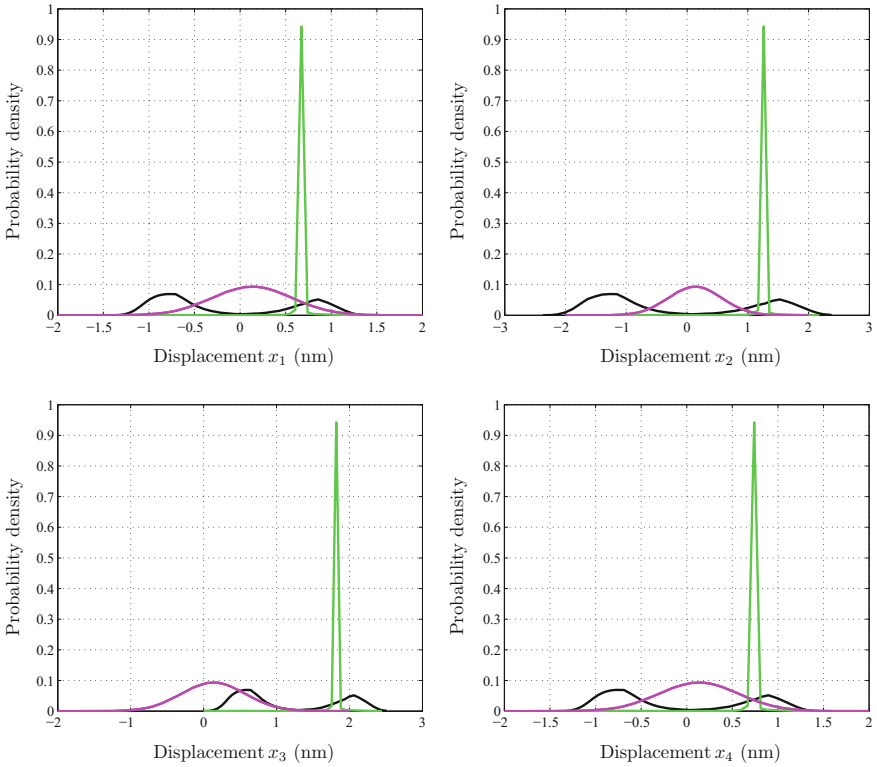


**Fig. 6.11** Probability density function of the displacements $x_i$ ($i = 1 \ldots 4$) for two values of noise intensities. For reference, the probability density of the noise driving signal is also plotted

## 6.9 Conclusions

In this chapter, we have considered the nonlinear dynamics of four identical coupled nanostructured graphene vibrating membranes for ambient energy applications at the nanoscale. The compressed graphene presents a nonlinearity that has been shown to play an important role in increasing the efficiency of this energy harvesting device by increasing the RMS values of the displacement and the velocity. We presented a continuous-time nonlinear dynamical model of the coupled system. When random vibrations are considered as the main ambient energy source for the system, the performances of the system as an energy harvester are presented in the steady- state nonequilibrium regime when the noise level for a certain value of the compression ratio. Although the study can be carried out for the system with the above-mentioned eighth-order potential, a simpler double-well fourth-order potential can be considered in order to inherit many available analytical results on the behavior of the Duffing

oscillator. Finally it should be noted that this structure of mechanically coupled graphene membranes is feasible and can physically fabricated. A possible way to get it is by suspending the membranes on a shared elastic anchors in a series configuration.

**Acknowledgments** This work was supported by the Spanish *ministerio de Economía y Competitividad* under grants DPI2013-47437-R and by the RUE CSD2009-00046 (Consolider-Ingenio 2010), FIS2009-12721-C04-03, FIS2012-37549-C05-05, ENE2009-14340-C02-02 and FP7-ICT-P.No.: 270005-ZEROPOWER.

## References

1. Kaźmierski, T. J., & Beeby, S. (Eds.) (2011). *Energy harvesting systems. Principles, modeling and applications*. Springer.
2. Neri, I., Travasso, F., Vocca, H., & Gammaitoni, L. (2011). Nonlinear noise harvesters for nanosensors. *Nano Communication Networks*, *2*(4), 230–234.
3. Gammaitoni, L., Vocca, H., Neri, I., Travasso, F., & Orfei, F. (2007). Vibration energy harvestng: linear and nonlinear oscillator approaches. In *Sustainable energy harvesting technologies-past, present and future* (pp. 171–190).
4. Tang, L., Yang, Y., & Soh, K. (2010). Toward broadband vibration-based energy harvesting. *Journal of Intelligent Material Systems and Structures*, *21*, 1867–1896. Dec.
5. Ralman, R., Brennan, M. J., Mace, B. R., & Kovacic, I. (2010). Potential benefits of a non-linear stiffness in an energy harvesting device. *Nonlinear Dynamics*, *59*, 545–558.
6. Trigona, C., Dumas, N., Latorre, L., Andò, B., Bagliom, S., & Nouet, P. (2011). Exploiting benfits of a periodically-forced nonlinear oscillator for energy harvesting from ambient vibration. *Procedia Engineering*, 2–4.
7. Liu, H., Tay, C. J., Quan, C., Kobayashi, T., & Lee, C. (2011). Piezoelectric MEMS energy harvester for low-frequency vibrations with wideband operation range and steadily increased output power. *Journal of Microelectromechanical Systems*, *20*(5), 1131–1142.
8. Xu, S., Qin, Y., Xu, C., Wei, Y., Yang, R., & Wang, Z. L. (2010). Self-powered nanowire devices. *Nature Nanotechnology*, *5*(5).
9. Wang, Z. L., Wang, X., Song, J., Liu, J., & Gao, Y. (2008). Piezoelectric nanogenerators for self-powered nanodevices. *Pervasive Computing*, *7*(1), 48–55.
10. Quin, Y., Wang, X., & Wang, Z. L. (2008). Microfibre-nanowire hybrid structure for energy scavenging. *Nature*, *451*(14), 809–813.
11. Wang, Z. L., Wang, X., Song, J., Liu, J., & Gao, Y. (2008). Piezoelectric nanogenerators for self-powered nanodevices. *Pervasive Computing, IEEE*, *7*(1), 49–55.
12. Imam, S. A., Sabri, S., & Szkopek, T. (2010). Low-frequency noise and hysteresis in graphene field-effect transistors on oxide S.A. *Micro and Nano Letters, IET*, *5*(1), 37–41.
13. Geim, A. K., & Novoselov, K. S. (2011). The rise of graphene. *Nature*, *6*(3), 183–191.
14. Brownson, D. A. C., Kampouris, D. K., & Banks, C. E. (2011). An overview of graphene in energy production and storage applications. *Journal of Power Sources*, *196*, 4873–4885.
15. Grande, L., Chundi, V. T., Wei, D., Bower, C., Andrew, P., & Ryhänen, T. (2011). Graphene for energy harvesting/storage devices and printed electronics. *Particuology*, *10*, 1–8.
16. Pumera, M. (2011). Graphene in biosensing. *Materials Today*, *14*(7–8), 308–315.
17. Singh, V., Joung, D., Zhai, L., Das, S., Khondaker, S. I., & Seal, S. (2011). Graphene based materials: Past, present and future. *Progress in Materials Science*, *56*, 1178–1271.
18. López-Suárez, M., Rurali, R., Gammaitoni, L., & Abadal, G. (2011). Nanostructured graphene for energy harvesting. *Physical Review B*, *84*(161401), 1–5.
19. Kwon, J., Sharma, B. K., & Ahn, J. -H. (2013). Graphene based nanogenerator for energy harvesting. *Japanese Journal of Applied Physics*, *52*(6S) 06GA02.

20. Dhiman, P., Yavari, F., Mi, X., Gullapalli, H., Shi, Y., Ajayan, P. M., et al. (2011). Harvesting energy from water flow over graphene. *Nano Letters*, *11*(8), 3123–3127.
21. Que, R., Shao, Q., Li, Q., Shao, M., Cai, S., Wang, S., et al. (2012). Flexible nanogenerators based on graphene oxide films for acoustic energy harvesting. *Angewandte Chemie International Edition*, *51*(22), 5418–5422.
22. El Aroudi, A., Lopez-Suarez, M., Rurali, R., Alarcon, E., & Abadal, G. (2013). Nonlinear dynamics in a nanostructured graphene device for energy harvesting applications. In *IEEE international symposium on circuits and systems, 2013, ISCAS 2013, May 2013, Beijing, China* (pp. 2727–2730).
23. El Aroudi, A., Lopez-Suarez, M., Rurali, R., Alarcon, E., & Abadal, G. (2014). Nonlinear dynamics of an ambient noise driven array of coupled graphene nanostructured devices for energy harvesting. In *A: International conference on structural dynamics and diagnosis. MATEC web of conferences* (Vol. 16); *CSNDD 2014: International conference on structural nonlinear dynamics and diagnosis*. *Agadir: EDP Sciences* (pp. 01001-1–01001-4).
24. Soler, J. M., Artacho, E., Gale, J. D., Garcıa, A., Junquera, J., Ordejon, P., & Sánchez-Portal, D. (2002). The SIESTA method for ab initio order-N materials simulation. *Journal of Physics: Condensed Matter*, *14*(11), 2745.
25. Gammaitoni, L., Neri, I., & Vocca, H. (2009). Nonlinear oscillators for vibration energy harvesting. *Applied Physics Letters*, *94*(16), 164102-1–164102-3.